

Cluster-Based Time-Variant Channel Characterization and Modeling for 5G-Railways

Xuejian Zhang, *Student Member, IEEE*, Ruisi He, *Senior Member, IEEE*, Bo Ai, *Fellow, IEEE*, Mi Yang, *Member, IEEE*, Jianwen Ding, *Member, IEEE*, Shuaiqi Gao, Ziyi Qi, Zhengyu Zhang, *Student Member, IEEE*, and Zhangdui Zhong, *Fellow, IEEE*

Abstract—With the development of high-speed railways, 5G for Railways (5G-R) is gradually replacing Global System for the Mobile Communications for Railway (GSM-R) worldwide to meet increasing demands. The large bandwidth, array antennas, and non-stationarity caused by high mobility has made 5G-R channel characterization more complex. Therefore, it is essential to develop an accurate channel model for 5G-R. However, researches on channel characterization and time-variant models specific to 5G-R frequency bands and scenarios is scarce. There are virtually no cluster-based time-variant channel models that capture statistical properties of 5G-R channel. In this paper, we propose a cluster-based time-variant channel model for 5G-R within an enhanced 3GPP framework, which incorporates time evolution features. Extensive channel measurements are conducted on 5G-R private network test line in China. We then extract and analyze typical channel fading characteristics and multipath cluster characteristics. Furthermore, birth-death process of the clusters is modeled by using a four-state Markov chain. Finally, a generalized clustered delay line (CDL) model is established in accordance with 3GPP standard and validated by comparing the results of measurements and simulations. This work enhances the understanding of 5G-R channels and presents a flexible cluster-based time-variant channel model. The results can be used in the design, deployment, and optimization of 5G-R networks.

Index Terms—5G-R, channel measurement, cluster-based channel model, time-variant characteristics.

I. INTRODUCTION

THE railway transportation system is widely acknowledged as an economical, energy-efficient, and effective mode of transporting goods and passengers [2]. The efficiency and reliability of railway transportation are fundamentally supported by railway wireless communication systems, which are crucial for the reliable transmission of key services and passenger safety [3], [4]. Over the past few decades, the Global System for Mobile Communications for Railway (GSM-R)

has been remarkably successful. While it is a narrowband system with low bandwidth and transmission rates, which no longer suffice to meet the escalating demands for train-ground private network services, such as train multimedia dispatch communications [5]–[7]. It is urgently needed to evolve into a new generation railway communication system.

With the full commercialization of 5G on public networks, applying 5G technology to railway systems, i.e. 5G for Railways (5G-R), has garnered substantial international interest. In Europe, under the auspices of the International Union of Railways (UIC), the Future Railway Mobile Communication System (FRMCS) has introduced 5GRAIL [8] as the successor to GSM-R. Railway companies in Japan and South Korea have deployed 5G infrastructure on select lines and conducted trials to verify communication performance in high-speed scenarios [9]. China is also shifting its research focus from GSM-R directly to 5G-R without considering Long-Term Evolution for Railway (LTE-R) [10]. In September 2023, the Ministry of Industry and Information Technology of China authorized the testing of 5G-R private network communication systems, designating the frequency band of 2100 MHz, i.e. uplink 1965–1975 MHz and downlink 2155–2165 MHz [11]. It is evident that advancing railway private network communication system into 5G era is imperative and has become a global consensus.

The study of radio wave propagation mechanisms and channel modeling is fundamental to the design and network planning of railway wireless communication systems [12]. Commonly employed link-level channel models include tapped delay line (TDL) and clustered delay line (CDL) models [13]. For 5G-R system, communication scenarios are considerably more complex [7], and the introduction of large bandwidth and multiple-input multiple-output (MIMO) provides the foundation for developing three-dimension (3D) wideband channel models [14]. More critically, 5G-R channel exhibits pronounced non-stationary characteristics due to high mobility of trains, which can be characterized by dynamic birth-death process of multipath clusters [15]. Thus it is imperative to establish a cluster-based time-variant 5G-R channel model to accurately reflect these characteristics.

Currently, a number of wireless channel studies for high-speed railways have emerged. Typical channel characteristics such as path loss (PL), shadow fading (SF), Rice K-factor based on GSM-R measurements in viaducts and cuttings at 930 MHz, are discussed and modeled in [16], [17]. Short-term fading behaviors in railway scenarios at 1.89 GHz and 2.605 GHz for LTE-R are analyzed in [18], [19]. A Markov-

Part of this paper is presented at the International Conference on Wireless Communications and Signal Processing (WCSP-2024) [1].

X. Zhang, R. He, B. Ai, J. Ding, S. Gao, Z. Qi, Z. Zhang, and Z. Zhong are with the School of Electronics and Information Engineering and the Frontiers Science Center for Smart High-speed Railway System, Beijing Jiaotong University, Beijing 100044, China (email: 23115029@bjtu.edu.cn; ruisi.he@bjtu.edu.cn; boai@bjtu.edu.cn; jwding@bjtu.edu.cn; 23120047@bjtu.edu.cn; 22115006@bjtu.edu.cn; 21111040@bjtu.edu.cn; zhdzhong@bjtu.edu.cn).

M. Yang is with the School of Electronics and Information Engineering and the Frontiers Science Center for Smart High-speed Railway System, Beijing Jiaotong University, Beijing 100044, China, and also with the Henan High-Speed Railway Operation and Maintenance Engineering Research Center, Zhengzhou 451460, China (e-mail: myang@bjtu.edu.cn).

based multi-link TDL for railway communications at 460 MHz is established in [20]. Refs. [21], [22] utilize measurement data in viaduct scenarios of LTE-R system to establish TDL models based on Markov chain, and [23] further extract the inter and intra-cluster parameters in time domain and delay domain. Ref. [11] introduces active and passive measurements based on 5G core network at 2100 MHz, discussing channel fading characteristics including PL and root mean square delay spread (RMS DS), and statistical model of PL for railway 5G marshalling yard scenario is discussed in [24]. Refs. [25] and [26] utilize ray tracing simulators to develop scenarios such as cutting, viaduct and equipment room at millimeter-wave frequencies and 2100 MHz, respectively, to investigate propagation characteristics.

Despite the considerable research focused on wireless channel within railway scenarios, most of existing work focuses on the analysis and modeling of specific channel characteristics, with the majority relying on TDL models. Although [23] proposed a CDL model, it is limited to two dimensions and lacks sufficient representation of angular domain. What's more, there is basically no research on 5G-R dedicated frequency bands and scenarios. To the best of our knowledge, the construction of 5G-R dedicated network is still in its infancy globally, dedicated frequency bands have not yet been issued in some countries and obtaining 5G-R channel measurement data remains highly challenging. Consequently, there is currently no established 5G-R time-variant channel model based on measurement data.

Instead, the more common approach involves employing geometry-based stochastic channel models (GBSMs) to construct CDL [27]. For instance, [28] proposed a 3D non-stationary massive MIMO GBSM based on the assumption of uniformly distributed scatterers, and a non-stationary small-scale fading model for 3D MIMO high-speed railway is established in [29]. Many standardization organizations also have extensively researched on GBSMs to support high-mobility scenarios, such as WINNER II [30], 3GPP TR 38.901 [31], COST 2100 [32], QuaDRiGa [33], and IMT-2020 [34]. However, these models still have certain limitations in meeting the specific technical requirements of 5G-R applications. For example, WINNER II, 3GPP TR 38.901, and IMT-2020 do not support the non-stationarity [29]. While GSM-based methods can partially describe non-stationarity of 5G-R channels, it lacks validation through field measurement data and fails to capture typical channel characteristics. Moreover, existing standards are insufficient in fully modeling channel in typical 5G-R scenarios, particularly with regard to non-stationarity.

In summary, current research on cluster-based 5G-R time-variant channels is highly inadequate, as reflected in the following aspects. First, conducting channel measurements for 5G-R systems is challenging, and the lack of essential measurement data makes it impossible to statistically model typical channel characteristics. Second, research on cluster-based 3D statistical channel models for high-speed railways is extremely limited, even beyond 5G-R systems, with minimal focus on 5G-R models that incorporate time-variation. Lastly, many standardization organizations have yet to provide detailed classifications for high-speed railway scenarios, particularly 5G-R

communication scenarios, and propose time-variant channel models considering non-stationarity for references.

To address the above gaps, we propose a cluster-based time-variant channel model for 5G-R within the 3GPP framework. Extensive channel measurements are conducted, from which we extracted typical 5G-R channel fading and cluster characteristics. The accuracy of proposed 5G-R channel model is subsequently validated against measured and simulated data. We have presented some preliminary experimental results in our previous work of [1]. Specifically, the main contributions of this paper are as follows:

- Comprehensive wideband MIMO 5G-R channel measurement campaigns are conducted in 5G-R private network test loop of China, yielding a substantial amount of measurement data.
- A cluster-based time-variant 5G-R channel model is proposed as an enhanced version of standard 3GPP framework. The model incorporates time evolution and characterizes non-stationarity by modeling the birth-death process of multipath clusters and dynamically updating cluster parameters.
- Typical 5G-R channel fading characteristics and multipath cluster characteristics are extracted and analyzed. Cluster lifetime and a first-order four-state Markov chain are employed to describe the cluster birth-death process.
- By comparing channel characteristic parameters between measurements, simulations and 3GPP model, the model implementation and validation are performed.

The remainder of this paper is organized as follows. Section II describes the framework of cluster-based 5G-R time-variant model based on 3GPP. Measurement system and scenarios are introduced in Section III. Then in Section IV, a series of channel characteristics are extracted and analyzed, and cluster characteristics and birth-death process are described in Section V. Section VI establishes a CDL model based on 3GPP standard and validates the model. Finally, Section VII draws the conclusions.

II. CLUSTER-BASED TIME-VARIANT MODEL FOR 5G-R CHANNELS

A. Channel Model Framework

Based on 3GPP TR 38.901 [31], we propose a generalized 5G-R channel model framework that more comprehensively captures non-stationary characteristics of wireless channels, as illustrated in Fig. 1. The current 3GPP framework does not discuss dynamic channels in detail, especially for smooth evolution of cluster characteristics. Although spatial consistency is introduced to make channel model more reflective of real-world mobile scenarios, it becomes insufficient in realistic dynamic environment with larger spatial and temporal scales [35]–[37]. With this in mind, we propose an improved version of 3GPP standard framework, i.e., adding “time evolution” part in Fig. 1. Channel generation procedure in this enhanced framework is divided into four key parts: general parameters, small-scale parameters, time evolution, and channel coefficient generation. They are introduced in detail below.

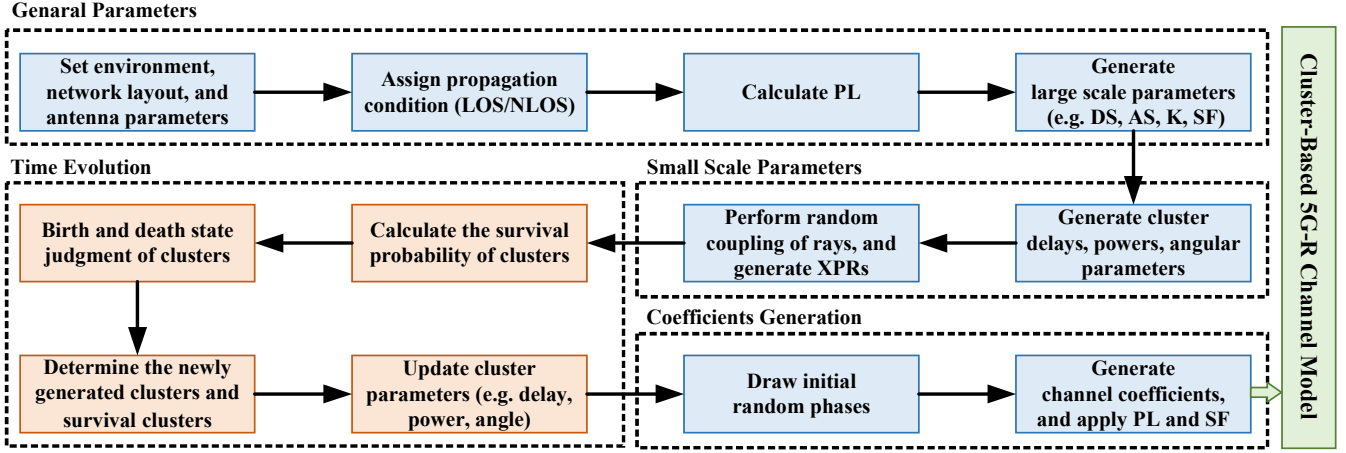


Fig. 1. Framework of non-stationary 5G-R channel modeling.

1) *General Parameters*: including initial setup of the whole system, and generate of corresponding PL model and large-scale parameters. Firstly, types of communication scenario, such as urban micro (UMi) and Rural macro (RMA), network layout and antenna parameters are chose and set, respectively. Specially, for base station (BS) and user terminal (UT), the number of antennas, 3D locations, antenna field patterns, array geometries, azimuth angle ϕ and elevation angle θ of each BS and UT in the global coordinate system need to be considered and determined. The speed and direction of UT motion, center frequency and bandwidth must be set, too. Then, propagation condition, i.e. line of sight (LOS) or non-line of sight (NLOS) can be assigned for different BS-UT links. Finally, the corresponding PL models with the formulas are formed and large scale parameters (LSPs) are calculated, including DS, AS, K-factor, SF, etc.

2) *Small Scale Parameters*: including a group of characteristics parameters of dynamic clusters, such as delays, powers, angular parameters. Small scale parameters of each individual cluster and rays within cluster are generated based on specific LSPs in general parameters and predefined statistical models in 3GPP [31]. Once all the per-ray powers, delays, and angles are obtained, then perform random coupling of rays within a cluster and apply cross polarization power ratios (XPRs). Furthermore, the full small scale parameters of clusters is obtained. Detailed generation process can be found in [31].

3) *Time Evolution*: Non-stationarity of the proposed channel model is embodied in two mechanisms, i.e., time-variant parameters and the birth-death process. Time-variant parameters are updated constantly and caused by birth-death process of clusters, while clusters in a specific scenario can exist over a certain time period, which means the number of clusters do not change frequently. Birth-death process can be modeled in many ways, such as statistical distribution of cluster lifetime and Markov chains. Here we follow the suggestions in [36], [38], [39] to formalize and generalize birth-death process to obtain probability of survival or death of each cluster.

Firstly, we define birth-death sampling interval as Δt_{BD} , and during the Δt_{BD} , cluster birth and death occurs. Temporal non-stationarity of 5G-R channel is most likely caused

by movement of UT as mentioned above, and the variable $\delta_P(t, \Delta t_{BD})$ is introduced to describe how much the propagation environment varies during the time interval between t and $t + \Delta t_{BD}$. It represents the sum of distances traveled by Tx and Rx from time t to $t + \Delta t_{BD}$ as

$$\delta_P(t, \Delta t_{BD}) = v_{UT}(t) \cdot \Delta t_{BD}, \quad (1)$$

where $v_{UT}(t)$ is the time-variant speed of UT. Note that, We consider all clusters having the same probability of survival. According to birth-death process, the clusters at time instant $t + \Delta t_{BD}$ are considered to be the sum of clusters that survive from moment t and the clusters that are generated at time intervals t_{BD} . The process is determined by a generation rate of clusters λ_G and a recombination rate of clusters λ_R . Consequently, the expectation of total number of clusters in the proposed channel model can be calculated as

$$E[N(t)] = \frac{\lambda_G}{\lambda_R}, \quad (2)$$

where $N(t)$ represents the time-variant number of clusters. The probabilities of clusters at $t + \Delta t_{BD}$ survived from t can be modeled as

$$P_{survival}(\Delta t_{BD}) = e^{-\lambda_R \cdot \frac{\delta_P(\Delta t_{BD})}{D_c}}, \quad (3)$$

where D_c is the scenario dependent correlation factor and typical values can be chosen in [39]. According to Poisson process, the durations between clusters appearance and disappearance follow exponential distribution. The expectation of the number of newly generated clusters can be computed as

$$E[N_{new}(t + \Delta t_{BD})] = \frac{\lambda_G}{\lambda_R} \left(1 - e^{-\lambda_R \cdot \frac{\delta_P(\Delta t_{BD})}{D_c}} \right). \quad (4)$$

In our proposed channel model, the disappearing clusters at each time instant are removed, while for the newly generated clusters, delays, powers and angle parameters are randomly generated which are similar to the previous steps. For the surviving clusters from previous time instant, the update process of delays, powers and angle parameters will be described in rest of this section.

4) *Coefficients Generation*: Draw random initial phase $\{\Phi_{n,m}^{\theta\theta}, \Phi_{n,m}^{\theta\phi}, \Phi_{n,m}^{\phi\theta}, \Phi_{n,m}^{\phi\phi}\}$ for each ray m of each cluster n and for four different polarisation combinations $\{\theta\theta, \theta\phi, \phi\theta, \phi\phi\}$, which are uniformly distributed in the range $(-\pi, \pi)$. Then channel impulse responses (CIRs) between u th UT and s th BS are generated based on 3GPP TR 38.901, which consists of two components, i.e., LOS component and NLOS component. For NLOS condition, CIR is

$$H_{u,s,n,m}^{NLOS}(t) = \sqrt{\frac{P_n}{M}} \begin{bmatrix} F_{rx,u,\theta}(\theta_{n,m,EOA}, \phi_{n,m,AOA}) \\ F_{rx,u,\phi}(\theta_{n,m,EOA}, \phi_{n,m,AOA}) \end{bmatrix}^T \begin{bmatrix} \exp(j\Phi_{n,m}^{\theta\theta}) \\ \sqrt{\kappa_{n,m}^{-1}} \exp(j\Phi_{n,m}^{\theta\phi}) \\ \sqrt{\kappa_{n,m}^{-1}} \exp(j\Phi_{n,m}^{\phi\theta}) \\ \exp(j\Phi_{n,m}^{\phi\phi}) \end{bmatrix} \begin{bmatrix} F_{tx,s,\theta}(\theta_{n,m,EOD}, \phi_{n,m,AOD}) \\ F_{tx,s,\phi}(\theta_{n,m,EOD}, \phi_{n,m,AOD}) \end{bmatrix} \exp\left(j2\pi \frac{\hat{r}_{rx,n,m}^T \cdot \bar{d}_{rx,u}}{\lambda_0}\right) \exp\left(j2\pi \frac{\hat{r}_{tx,n,m}^T \cdot \bar{d}_{tx,s}}{\lambda_0}\right) \cdot \exp\left(j2\pi \frac{\hat{r}_{rx,n,m}^T \cdot \bar{v}_{UT}}{\lambda_0} t\right) \quad (5)$$

where $F_{rx,u,\theta}$, $F_{rx,u,\phi}$, $F_{tx,s,\theta}$, $F_{tx,s,\phi}$ are the field patterns of the u th UT and s th BS in the direction of spherical basis vector, respectively; $\kappa_{n,m}$ is the XPR for m th ray of n th cluster; $\hat{r}_{rx,n,m}$ and $\hat{r}_{tx,n,m}$ denote the spherical unit vector with its corresponding azimuth arrival angle and elevation arrival angle, while $\bar{d}_{tx,s}$ and $\bar{d}_{rx,u}$ denote the location vector at the antennas of BS and UT respectively; λ_0 is the wavelength of carrier frequency and M is the number of rays within the cluster; \bar{v}_{UT} is the timeinvariant velocity of UT.

For LOS condition, CIR of the LOS path is given as

$$H_{u,s,1}^{LOS}(t) = \begin{bmatrix} F_{rx,u,\theta}(\theta_{LOS,EOA}, \phi_{LOS,AOA}) \\ F_{rx,u,\phi}(\theta_{LOS,EOA}, \phi_{LOS,AOA}) \end{bmatrix}^T \begin{bmatrix} 1 & 0 \\ 0 & -1 \end{bmatrix} \begin{bmatrix} F_{tx,s,\theta}(\theta_{LOS,EOD}, \phi_{LOS,AOD}) \\ F_{tx,s,\phi}(\theta_{LOS,EOD}, \phi_{LOS,AOD}) \end{bmatrix} \exp\left(j2\pi \frac{\hat{r}_{rx,LOS}^T \cdot \bar{d}_{rx,u}}{\lambda_0}\right) \exp\left(j2\pi \frac{\hat{r}_{tx,LOS}^T \cdot \bar{d}_{tx,s}}{\lambda_0}\right) \exp\left(j2\pi \frac{\hat{r}_{rx,LOS}^T \cdot \bar{v}_{UT}}{\lambda_0} t\right) \exp\left(-j2\pi \frac{d_{3D}}{\lambda_0}\right) \quad (6)$$

where d_{3D} is the 3D distance between BS and UT. Note that, CIR of LOS condition is the sum of CIRs of LOS path and NLOS condition with the scaling based on K-factor K_R , given by

$$H_{u,s}^{LOS}(\tau, t) = \sqrt{\frac{1}{K_R+1}} H_{u,s,n,m}^{NLOS}(\tau, t) + \sqrt{\frac{K_R}{K_R+1}} H_{u,s,1}^{LOS}(t) \delta(\tau - \tau_1) \quad (7)$$

where $\delta(\cdot)$ is the Dirac's delta function. The LOS component is associated with the shortest possible delay of all τ_n , i.e., τ_1 . As final step, path loss and shadowing are applied for all channel coefficients.

B. Cluster Parameters Evolution

On a time scale, cluster parameters will be dynamically updated due to the movement of BS or UT. To fully characterize non-stationarity of dynamic channel, it is particularly important to be able to update time-variant cluster parameters [40]. Note that, this paper does not study the scenario of train-to-train communications. Therefore, for typical high-speed railway scenarios, BS is fixed, and scatterers around

the railway, such as high-rise buildings, mountains, cuts, can also be considered fixed. Pedestrians and regular vehicles rarely appear around railways, and their impact on 5G-R channels is relatively small. Given the specific characteristics of 5G-R railway communication, and drawing on the standards established by 3GPP [31], IMT-2020 [34], WINNER II [30], as well as previous work on non-stationary channel models [35], [36], [38], we model the update process of cluster delay, power, and angle parameters.

1) *Update Delays*, $\tau_n(t)$. At moment $t_k = t_{k-1} + \Delta t$, the delay of the n th cluster is given as

$$\tilde{\tau}_n(t_k) = \tilde{\tau}_n(t_{k-1}) - \frac{\hat{r}_{rx,n}(t_{k-1})^T \bar{v}(t_{k-1})}{c} \Delta t, \quad (8)$$

where c is the speed of light, $\bar{v}(t_{k-1})$ is UT velocity vector in 3D and given as

$$\bar{v}(t_{k-1}) = [V_X(t_{k-1}) \quad V_Y(t_{k-1}) \quad V_Z(t_{k-1})]^T \quad (9)$$

After updating the delays according to Equation (8), the delays over the mobility range are normalized. Thus the final delay set is

$$\tau_n(t_k) = \tilde{\tau}_n(t_k) - \min\{\tilde{\tau}_n(t_k)\}, \quad (10)$$

where t_k covers the entire duration of dynamic channel.

2) *Update Powers*, $P_n(t)$. After obtaining delay of update completion of the n th cluster at moment t_k , power update only needs to substitute Equation (10) into

$$P_n^* = \exp\left(-\tau_n \frac{r_\tau - 1}{r_\tau \cdot DS}\right) \cdot 10^{-Z_n/10}, \quad (11)$$

where P_n denotes cluster power, $Z_n \sim N(0, \zeta^2)$, ζ represents the per-cluster shadowing and can be found in [31].

3) *Update Angle Parameters*. For the n th cluster, define rotation matrix R to transfer $\bar{v}(t_{k-1})$ to $\bar{v}^*(t_k - 1)$:

$$\begin{aligned} \bar{v}^*(t_k - 1) &= R \cdot \bar{v}(t_k - 1) \\ &= [V_X^*(t_{k-1}) \quad V_Y^*(t_{k-1}) \quad V_Z^*(t_{k-1})]^T, \end{aligned} \quad (12)$$

where the definitions of R in the standards are different for LOS and NLOS clusters, and a detailed introduction can be found in [31]. Now, Cluster departure angles and arrival angles in radians are updated as

$$\frac{\phi_{n,AOD}(t_k) - \phi_{n,AOD}(t_{k-1}) + \bar{v}^*(t_{k-1})^T \cdot \hat{\phi}(\theta_{n,EOD}(t_{k-1}), \phi_{n,AOD}(t_{k-1}))}{c \cdot \tilde{\tau}_n(t_{k-1}) \cdot \sin(\theta_{n,EOD}(t_{k-1}))} \Delta t, \quad (13)$$

$$\frac{\theta_{n,EOD}(t_k) - \theta_{n,EOD}(t_{k-1}) + \bar{v}^*(t_{k-1})^T \cdot \hat{\theta}(\theta_{n,EOD}(t_{k-1}), \phi_{n,AOD}(t_{k-1}))}{c \cdot \tilde{\tau}_n(t_{k-1})} \Delta t, \quad (14)$$

$$\frac{\phi_{n,AOA}(t_k) - \phi_{n,AOA}(t_{k-1}) + \bar{v}^*(t_{k-1})^T \cdot \hat{\phi}(\theta_{n,EOA}(t_{k-1}), \phi_{n,AOA}(t_{k-1}))}{c \cdot \tilde{\tau}_n(t_{k-1}) \cdot \sin(\phi_{n,EOA}(t_{k-1}))} \Delta t, \quad (15)$$

$$\frac{\theta_{n,EOA}(t_k) - \theta_{n,EOA}(t_{k-1}) + \bar{v}^*(t_{k-1})^T \cdot \hat{\theta}(\theta_{n,EOA}(t_{k-1}), \phi_{n,AOA}(t_{k-1}))}{c \cdot \tilde{\tau}_n(t_{k-1})} \Delta t, \quad (16)$$

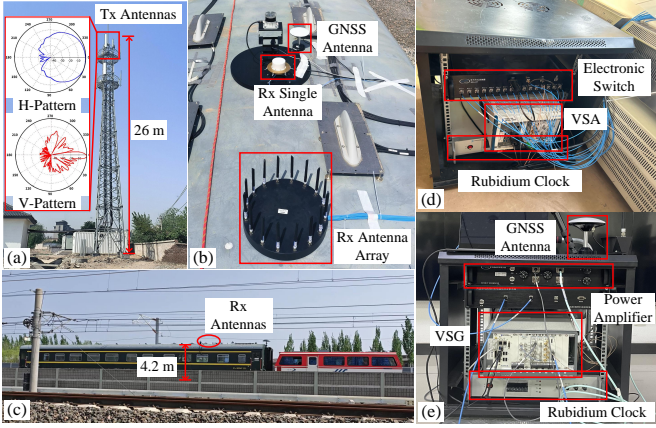


Fig. 2. Measurement Equipments. (a) BS and Tx antennas; (b) On-board roof Rx antennas; (c) Test train; (d) Primary equipments of Tx; (e) Primary equipments of Rx.

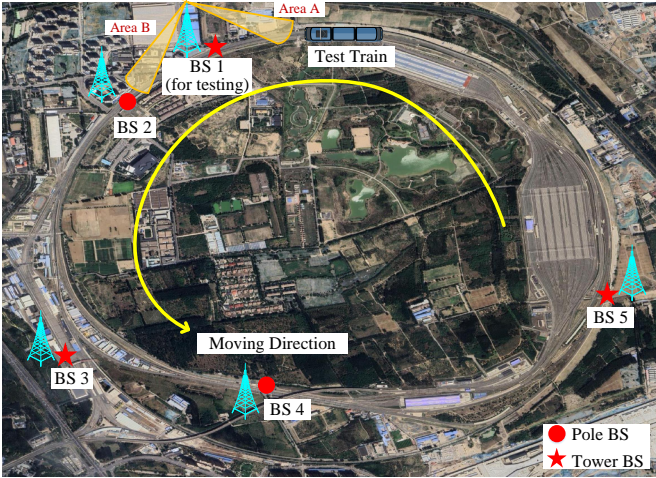


Fig. 3. Measurement scenario: loop railway test line.

where $\hat{\theta}(\theta, \phi)$ and $\hat{\phi}(\theta, \phi)$ are the spherical unit vectors defined in [31] as

$$\hat{\theta} = \begin{bmatrix} \cos \theta \cos \phi \\ \cos \theta \sin \phi \\ -\sin \theta \end{bmatrix}, \hat{\phi} = \begin{bmatrix} -\sin \phi \\ +\cos \phi \\ 0 \end{bmatrix}. \quad (17)$$

So far, through the above steps we complete the update of surviving cluster parameters within time interval Δt_{BD} . For the newly generated clusters, their parameters are randomly generated according to the generation process of small scale parameters in Section II-(A).

III. MEASUREMENT CAMPAIGN

A. Measurement System

The key equipment in the measurements is shown in Fig. 2. The measurement system comprises transmitting (Tx) and receiving (Rx) subsystems, with the core components being a vector signal generator (VSG) and a vector signal analyzer (VSA). Both VSG and VSA are based on National Instruments (NI) equipment. Specifically, NI PXIe-5673, NI PXIe-5663, and USRP 2954 are utilized as VSG and VSAs, respectively.

TABLE I
CONFIGURATION OF 5G-R CHANNEL MEASUREMENT SYSTEM.

| Parameters | Description |
|----------------------------|---|
| Center Frequency | 2160 MHz |
| Bandwidth | 10 MHz |
| Number of frequency points | 513 |
| Tx antennas | $\pm 45^\circ$ directional panel antennas |
| Rx antennas | Vertical polarized omni-directional 16-element circular array and biconical antenna |
| Transmitting Power | 43 dBm |
| Sampling rate | 500 snapshots/s with single antenna (one snapshot per 0.32λ) 16 snapshots/s with circular array (one snapshot per 10λ) |
| Height of antenna | 26 m (Tx antennas) 4.2 m (Rx antennas) |
| Antenna gain | 17.5 dBi (Tx antennas) 3 dBi (Rx antennas) |
| Length of loop line | 9 km |
| BS feeder loss | 4.1 dB |
| Speed of locomotive | 80 km/h |

Tx antennas are $\pm 45^\circ$ polarized directional panel antenna with gain of 17.5 dBi. They are installed on a tower with height of 26 m, as shown in Fig. 3 (a), which also contains antenna patterns. To realize measurements of small-scale fading and angle domain at the same time, 16-element circular array and single conical antenna are deployed at Rx and controlled by NI PXIe-5663 and USRP-2954, respectively, both of which are vertically polarized omnidirectional antennas with gain of 3 dBi. They can simultaneously receive multi-antenna data with 16 snapshots/s and single-antenna data with 500 snapshots/s. Rx antennas are magnetically attached to the top of test train at height of 4.2 m, as depicted in Figs. 2(b) and (c).

Except antennas, other key equipment is housed in two 12U cabinets, as shown in Figs. 2(d) and (e). Rx cabinet is placed inside test train, while Tx cabinet is located in equipment room under the tower. Power amplifier provides a maximum gain of 43 dB with an adjustable step of 1 dB. Electronic switch enables millisecond-level fast switching between 16 sub-channels to control circular array, implementing single-transmit multiple-receive (SIMO) based on time division multiplexing. To ensure time synchronization, two rubidium clocks tamed by Global Navigation Satellite System (GNSS) signals are employed. Additionally, rubidium clocks can also output longitude and latitude coordinates, allowing us to obtain real-time position information of Tx and Rx. Detailed measurement system configuration is shown in Table I.

B. Measurement Scenario

Measurement campaign is carried out at the National Railway Track Test Center, located northeast of Beijing, China. It features the largest loop railway test line in Asia, spanning a total length of approximately 9 km [11]. Along this railway, five 5G-R dedicated network base stations (BSs) have

been constructed, equipped with BS equipment from multiple manufacturers, which are illustrated in Fig. 3.

During the measurements, Tx cabinet is connected to Tx antennas of BS 1 to radiate vector signals outward, with carrier frequency of 2160 MHz and bandwidth of 10 MHz. This setup complies with 5G-R dedicated test frequency band issued by the Ministry of Industry and Information Technology of China. It is important to note that only two Tx antennas with opposite radiation directions are used to cover Areas A and B, as shown in Fig. 3. It can be seen that in Area A, there are basically no abundant residential buildings, only a few large facilities along the railway, such as train control center, operation and maintenance building, and the scatterers are relatively sparse; while in Area B, more residential houses and low buildings are present, the scatterers are denser. What's more, to eliminate signal interference from public network and inter-station, frequency band of 2155-2165 MHz is cleared, and all BSs except BS 1 are shut down.

Test train consists of a locomotive and a carriage, as shown in Fig. 2(c). It maintains a speed of 80 km/h and moves counterclockwise along the circular railway line for several laps to ensure that sufficient channel data is obtained. The measured environment can be classified as a rural area, characterized by surrounding trees and sparse low-rise buildings. Additionally, specific railway objects, such as low partition walls and contact network poles along the railway, are present in the measurement environment.

C. System Calibration and Data Processing

Measurement system calibration is a crucial step in ensuring accurate results. It consists of back-to-back measurement and antenna calibration. Back-to-back measurement refers to directly connecting Tx and Rx via a radio frequency cable and several attenuators without involving wireless channel. It effectively compensates for amplitude-frequency response caused by cables, adapters, transceivers, etc. Moreover, Tx and Rx antennas have been accurately measured in an anechoic chamber for radiation patterns. This allows for the correction of errors introduced by antenna radiation characteristics during data processing, known as antenna calibration.

Channel impulse response $h(t, \tau)$ can be obtained by calculating channel transfer function in frequency domain after considering system calibration and then performing a Fourier transform on it, where t is index of measurement time snapshot, τ is delay bin. Detailed description can be found in [41].

IV. CHANNEL CHARACTERISTICS

In this section, we extract and analyze typical channel characteristics based on single-antenna measured data, such as PL, SF, power delay profile (PDP), RMS DS, K-factor, and stationary region.

A. Path Loss and Shadow Fading

PL and SF are large-scale propagation characteristics, which can be determined by averaged channel gain as follows

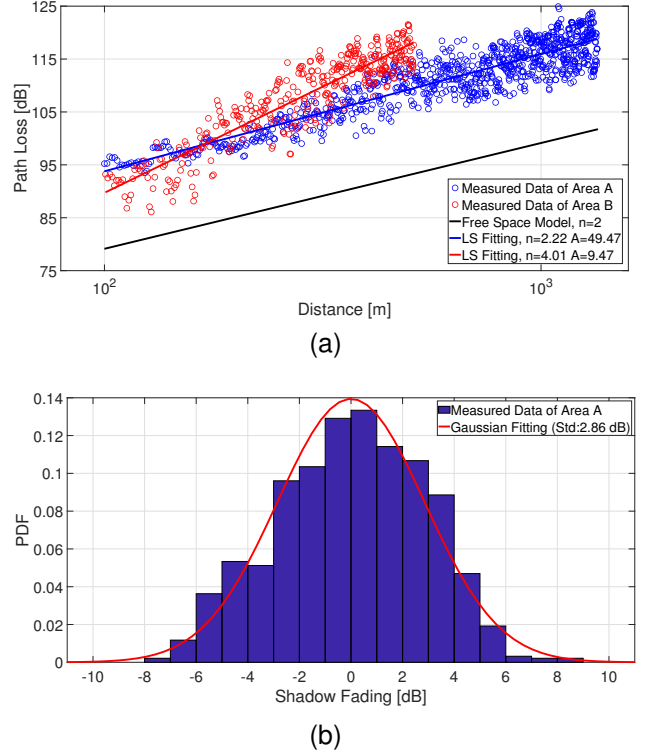


Fig. 4. (a) Measured PL with the corresponding Log-distance fitting. (b) Measured SF and Gaussian fitting.

$$L = -10 \log_{10} \left(\frac{1}{W} \sum_{T=t-\frac{W}{2}}^{t+\frac{W}{2}-1} \sum_{\tau=1}^{N_f} |h(T, \tau)|^2 \right). \quad (18)$$

where N_f is the number of measured frequency points, L is large-scale components in dB-scale including PL and SF, and W is a 40λ sliding window, λ denotes wavelength. After eliminating small-scale fading by a sliding window of 40λ , the dB-valued PL and SF can be generally modeled as [42]

$$L(d) = A + 10n \log_{10} \left(\frac{d}{d_0} \right) + X_\sigma, \quad (19)$$

where A is intercept value and n is path loss exponent, d and d_0 represents the distance between Tx and Rx and the reference distance which set to 1 m, respectively. SF is represented by X_σ , which is a zero-mean Gaussian distributed random variable with standard deviation σ .

The measured distance-dependent path loss and the corresponding linear fitting with Least Square (LS) regression in Areas A and B are shown in Fig. 4(a). For eliminating near-field effect caused by antenna directivity, we ignore the data within first 100 m. The observed disparity in path loss between Areas A and B is minimal, with n of 2.22 and 4.01, respectively. However, both areas exhibit path loss values approximately 20 dB higher than free space model. This deviation is attributable to various scatterers present in measurement environment, including low-rise buildings, trees, platforms, utility poles, etc. What's more, it can be seen from Fig. 3 that area A is relatively open with fewer scattering objects, characterized mainly by occasional railway infrastructure and sparse tree

TABLE II
SUMMARY OF CHANNEL CHARACTERISTIC PARAMETERS.

| Parameters | Statistical Distribution | Description | Value | |
|----------------------|---|-------------|-----------------|--------------|
| | | | Area A | Area B |
| PL | Linear | n A | 2.22 49.47 | 4.01 9.47 |
| SF | Gaussian $N(0, 2.86^2)$ $N(0, 3.40^2)$ | Std. | 2.86 dB | 3.40 dB |
| RMS DS | Lognormal $N(4.33, 0.39^2)$ | Mean | 81.79 ns | |
| | | Std. | 34.39 ns | |
| Rice K-factor | Normal $N(0.66, 2.78^2)$ $N(-1.22, 3.22^2)$ | Mean | 0.66 dB | -1.22 dB |
| | | Std. | 2.78 dB | 3.22 dB |
| ASA | Lognormal $N(1.78, 1.45^2)$ | Mean | 16.26° | |
| | | Std. | 25.19° | |
| ESA | Lognormal $N(0.48, 0.65^2)$ | Mean | 2.37° | |
| | | Std. | 1.91° | |
| Cluster lifetime | Lognormal $N(0.88, 0.92^2)$ | Mean | 3.74 s | |
| | | Std. | 4.57 s | |
| Stationary Region | Lognormal $N(2.16, 0.29^2)$ | Mean | 9.02 m / 0.41 s | |
| | | Std. | 2.51 m / 0.11 s | |

cover. Consequently, n for area A approaches theoretical free-space value of 2. In contrast, area B is characterized by a higher density of buildings, contributing to a marginally higher path loss and a correspondingly larger path loss exponent.

Take the result of area A as example, probability density functions (PDFs) of SF is illustrated in Fig. 4(b). The statistical parameters are listed in Table II. Standard deviations of areas A and B are 2.86 dB and 3.40 dB, respectively. It can be seen that shadow fading can be well fitted to a zero-mean Gaussian distribution. Additionally, standard deviation in area B exhibits greater variability compared to area A, which aligns with the results depicted in Fig. 4(a).

B. Power Delay Profile and Delay Spread

PDP is extensively employed to characterize the power levels of received paths with propagation delays and to describe the distribution of multi-path components (MPCs) in measured environments. The instantaneous PDP is denoted as

$$P(t, \tau) = |h(t, \tau)|^2. \quad (20)$$

To achieve more precise analysis results, a fixed noise threshold is used to eliminate noise components, and the noise threshold is set to 6 dB above the background noise floor. Only signals exceeding this noise threshold are deemed valid, while samples below the threshold are set to zero. Fig. 5 illustrates average PDPs (APDPs), obtained by averaging with a sliding window of 40λ .

APDPs depicted in Fig. 5 aligns closely with actual measurement scenario. As test train approaches BS and subsequently moves away, the delay of LOS path correspondingly decreases and then increases. The power of LOS reaches peaks when train is closest to BS. Notably, MPCs are prominently observed only for a brief duration near BS. This is attributed to the stronger MPCs having more substantial reflection and scattering off objects such as tower, equipment room and trains during this period, while in other delay bins, LOS

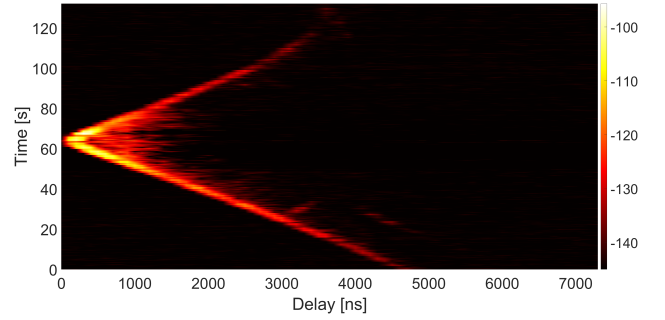


Fig. 5. Measured APDP.

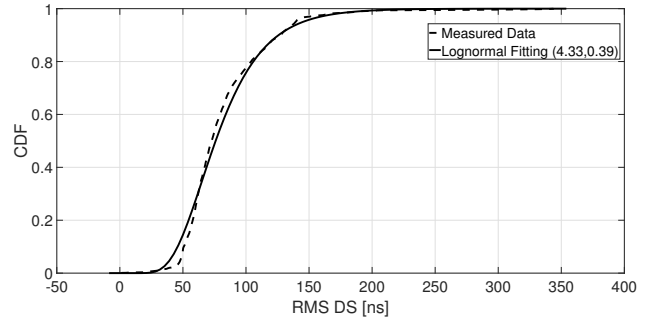


Fig. 6. Measured RMS DS and Lognormal fitting.

propagation predominates. This observation can be explained by two factors: firstly, measurement environment is a rural area with sparse scattering objects and limited MPCs; secondly, measurement bandwidth is only 10 MHz, resulting in a delay resolution of 100 ns. The low delay resolution restricts the ability to distinguish more MPCs.

RMS DS is the square root of the second central moment of APDPs and is widely used to characterize the delay dispersion of channels. It is defined as

$$\tau_{rms}(d) = \sqrt{\frac{\sum_p APDP(d, \tau_p) \tau_p^2}{\sum_p APDP(d, \tau_p)} - \left(\frac{\sum_p APDP(d, \tau_p) \tau_p}{\sum_p APDP(d, \tau_p)}\right)^2}, \quad (21)$$

where τ_p represents the delay of the p th path and $APDP(d, \tau_p)$ describes the corresponding power with τ_p measured at location d .

The measured results and cumulative probability functions (CDFs) of RMS DS are shown in Fig. 6, and statistical results are summarized in Table II. It can be found that RMS DS follows a Lognormal distribution, with a mean of 81.79 ns and a standard deviation of 34.39 ns. For 90% of time, RMS DS remains below 128 ns, while it fluctuates between 150 and 345 ns only for brief periods near BS. This phenomenon occurs because proximity to BS results in more abundant MPCs, leading to greater delay spread. Conversely, in instances where LOS propagation is predominant, delay spread is relatively small. These findings are highly consistent with those illustrated in Fig. 5.

C. Rice K-factor

Rice K-factor represents the ratio of the power of LOS component and the power of NLOS component in the channel [43], which can be calculated based on APDP. The calculation formula is as follow

$$K = \frac{|h_{LOS}|^2}{\sum_{\tau} |h_{NLOS}|^2}, \quad (22)$$

where h_{LOS} is LOS component, and h_{NLOS} is NLOS component. All valid multipaths in APDPs are identified using multipath discrimination algorithm [44]. The multipath with the highest power in single snapshot is designated as h_{LOS} , while the remaining valid multipaths are classified as h_{NLOS} .

Rice K-factor derived from full-range measured data is depicted in Fig. 7(a). BS is located at the origin (distance equals zero), Area A spans from -1500 to 0 m, and Area B extends from 0 to 1500 m. Fig. 7(a) indicates that K-factor generally increases as the distance decreases, implying a higher proportion of power from LOS. However, a sharp decline is observed directly below BS as shown the red circles, attributed to near-shadow area caused by antenna directivity. Figs. 7(b) presents the corresponding CDFs and Normal distribution fitting of K-factor in two areas. It can be seen that K-factor follows a Normal distribution, with mean and standard deviation values in areas A and B being 0.66, 2.78 dB and -1.22, 3.22 dB, respectively. The smaller mean and larger standard deviation in area B imply a greater proportion of NLOS components and more significant fluctuations, consistent with the observations in Fig. 7(a).

D. Stationary Region

The rapid movement of high-speed train causes channel non-stationarity. In this paper, the temporal PDPs correlation coefficient (TPCC) is used as a measure of channel stationarity. The temporal similarity of PDPs between different times can be quantified by this metric. The TPCC between the PDPs at time t_i and t_j can be computed as

$$c(t_i, t_j) = \frac{\int P(t_i, \tau) \cdot P(t_j, \tau) d\tau}{\max\{\int P^2(t_i, \tau) d\tau, \int P^2(t_j, \tau) d\tau\}}. \quad (23)$$

The values of TPCCs are normalized from 0 to 1, and a high TPCC value indicates that the channel has higher similarity between t_i and t_j , as shown in Fig. 8(a). What's more, a threshold needs to be selected to determine stationary region window ΔW . Following the recommendation of [50], 0.8 is chosen as threshold. For a TPCC between t_i and t_j , when $c(t_i, t_j)$ is large than the threshold, the channel is considered not to experience significant change. Then ΔW between t_i and t_j can be obtained from TPCCs by using the threshold. Further, we calculates the stationarity distance by using the relationship between time, distance, and velocity. Fig. 8(b) statistics the CDFs of stationarity distance for measured data and Lognormal fitting. The average values and standard deviation of stationarity distance are 9.02 m and 2.51 m respectively, and the corresponding ΔW is 0.41 s and 0.11 s.

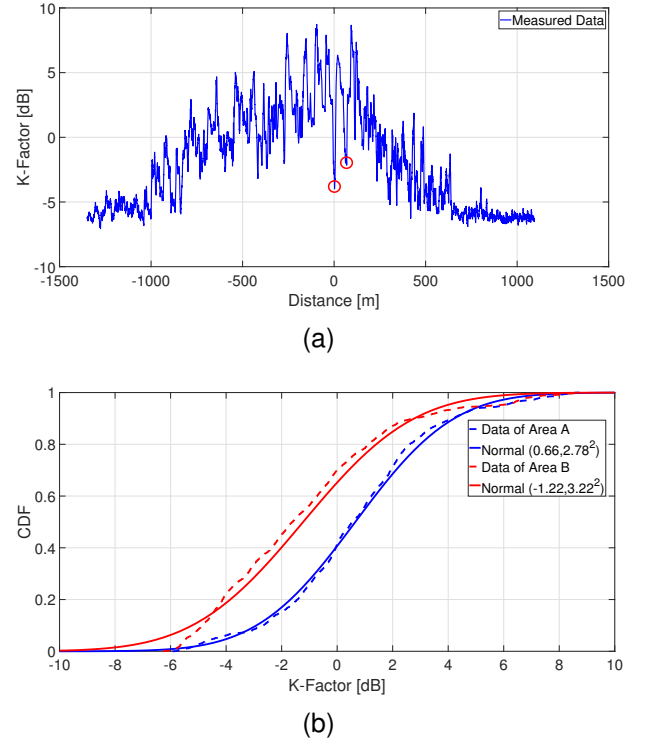


Fig. 7. Measured Rice K-factor and corresponding fitting. (a) Rice K-factor based on all measured data. The distance equal to 0 represents the location of BS, the range of distance [-1500,0] is area A, and the opposite is area B. (b) CDFs of Rice K-factor and Normal fitting of areas A and B.

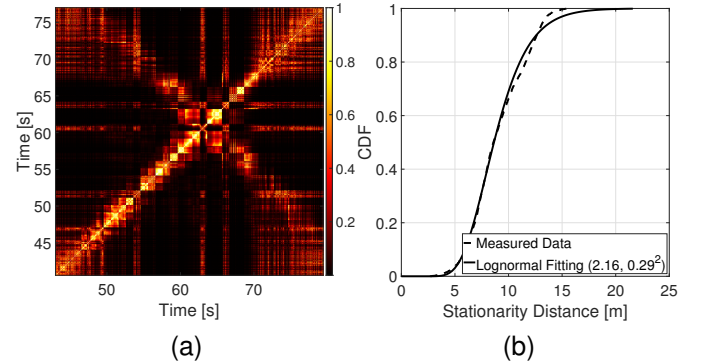


Fig. 8. TPCCs and stationarity distance. (a) TPCCs; (b) CDFs of stationarity distance.

V. MULTIPATH CLUSTER CHARACTERISTICS

In this section, we extract and analyze multipath clusters characteristics based on multi-antenna data, focusing on estimating MPC parameters using the Space-Alternating Generalized Expectation-Maximization (SAGE) algorithm and identifying and tracking clusters with KPowerMeans and multipath component distance (MCD)-based tracking algorithms. It is important to note that at greater distances from BS, the signal-to-noise ratio of multi-antenna receiver is lower compared to that of single-antenna receiver. As a result, although measured simultaneously, effective measurement duration for multi-antenna data are shorter, approximately 65 s and 1000 snapshots, while single-antenna data extends to around 123 s.

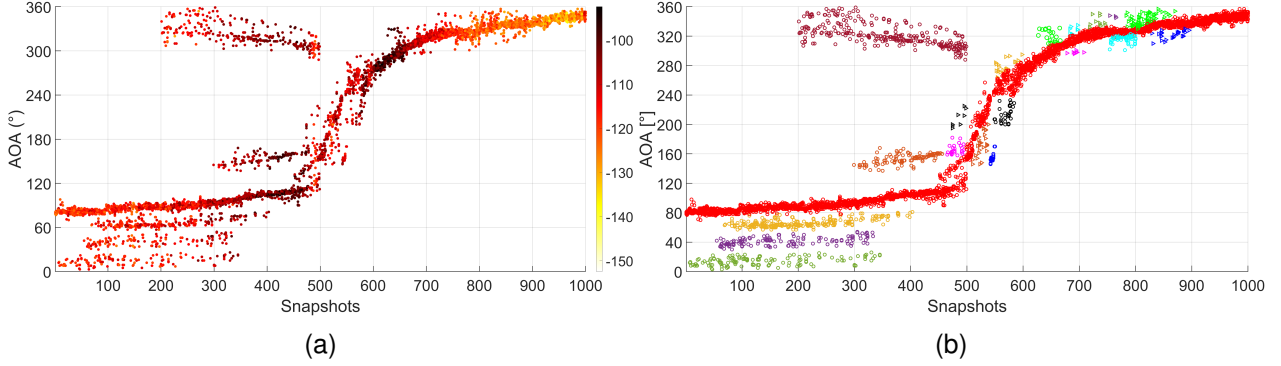


Fig. 9. (a) Angle estimation results of AOA. (b) Cluster identification and tracking results.

A. Estimation of MPCs Parameters

As the antenna array is only utilized at Rx and not at Tx, we are limited to obtaining arrival angle information. It is important to note that we utilize a circular array, with AOA and EOA calculated based on steering vector within the ranges of $[0^\circ, 360^\circ]$ and $[0^\circ, 90^\circ]$, respectively. The SAGE algorithm is employed to extract MPC parameters, including power, delay, AOA and EOA, i.e. $\{\alpha, \tau, \phi, \theta\}$. The SAGE algorithm provides a maximum-likelihood estimate of the MPC parameters through an iterative process, which has been widely applied to MPC identification and parameter estimation. Then the angular resolution of MPC angle estimation result obtained by SAGE algorithm in this paper is 2° . Detailed description of SAGE algorithm can be found in [41].

The amplitude and angle of arrival of MPCs derived from measured data are illustrated in Fig. 9(a). It is observed that as Rx gradually approaches and then moves away from BS, AOA of LOS component changes from 80° to 360° , consistent with the findings in [18]. Notably, around the 450-th to 600-th snapshots, Rx passes directly beneath BS, causing AOA to become discretized due to the presence of near-shadow area. Additionally, several distinct MPC clusters, resulting from large buildings adjacent to the railway in the measurement environment, are observed besides LOS component. Conversely, EOA generally exhibits minor fluctuations around 50° to 80° , except for a brief peak when approaching and moving away from BS. The fluctuations EOA are not demonstrated here, but can be seen in previous work [1].

RMS AS is defined as the second moment of angular power spectrum and is typically used to describe angular dispersion of channel. It is widely used to represent the discreteness of arrival/departure angles, and can be calculated as

$$AS = \sqrt{\frac{\sum_{l=1}^L (\Psi_{Angle,l} - \mu_{APS})^2 \alpha_l^2}{\sum_{l=1}^L \alpha_l^2}}, \quad (24)$$

where L is the total number of all MPCs. Parameters $\Psi_{Angle,l}$ and α_l represent arrival angle and complex amplitude of the l th MPC, respectively. Parameter μ_{APS} is the mean of angular power spectrum and

$$\mu_{APS} = \frac{\sum_{l=1}^L \Psi_{Angle,l} \alpha_l^2}{\sum_{l=1}^L \alpha_l^2}. \quad (25)$$

Statistical parameters of ASA and ESA are listed in Table II. ASA and ESA generally conform to Lognormal distribution, with means and standard deviations being 16.26° , 25.19° and 2.37° , 1.91° , respectively. Among them, the mean and standard deviation of ASA are much larger than those of ESA, which indicates that diffusion degree of AOA is greater.

B. Identification and Tracking of MPCs Clusters

Based on MPCs parameter estimations, clustering and tracking algorithm are used to identify time-variant clusters of MPCs. As an evolved algorithm of KMeans and incorporating the MPC power as the weight [45], classical KPowerMeans algorithm is employed to cluster MPCs in this paper. A detailed description of KPowerMeans algorithm can be found in [46]. Subsequently, we apply a MCD-based tracking algorithm to identify and track time-variant MPC clusters across multiple snapshots. For two arbitrary MPCs P_x and P_y in consecutive snapshots Ω_i and Ω_{i+1} , the MPCs' information can be expressed as [47], [48]

$$\begin{aligned} P_x \in \Omega_i &: [\alpha_x(i); \tau_x(i); \phi_x(i); \theta_x(i)], \\ P_y \in \Omega_{i+1} &: [\alpha_x(i+1); \tau_x(i+1); \phi_x(i+1); \theta_x(i+1)]. \end{aligned} \quad (26)$$

The MCD of two MPCs in angle domain can be expressed as

$$MCD_{angle,xy} = \frac{1}{2} \left| \begin{pmatrix} \cos(\phi_x) \sin(\theta_x) \\ \sin(\phi_x) \sin(\theta_x) \\ \cos(\theta_x) \end{pmatrix} - \begin{pmatrix} \cos(\phi_y) \sin(\theta_y) \\ \sin(\phi_y) \sin(\theta_y) \\ \cos(\theta_y) \end{pmatrix} \right|. \quad (27)$$

The MCD of delay is obtained as

$$MCD_{delay,xy} = \xi \cdot \frac{\tau_{std}}{\Delta\tau_{max}} \cdot \frac{|\tau_x - \tau_y|}{\Delta\tau_{max}}, \quad (28)$$

where

$$\Delta\tau_{max} = \max(\tau_n) - \min(\tau_n), n \in (\Omega_i \cup \Omega_{i+1}) \quad (29)$$

and τ_{std} is a standard deviation for the delays of $\Omega_i \cup \Omega_{i+1}$. Parameter ξ is scaling factor used to adjust the weight of $MCD_{delay,xy}$ in the overall MCD MCD_{xy} . And MCD_{xy} can be expressed as follow

$$MCD_{xy} = \sqrt{\|MCD_{angle,xy}\|^2 + MCD_{delay,xy}^2}. \quad (30)$$

MCD measures the similarity between two MPCs, i.e. smaller value means that two MPCs are more similar. What's more, a specified threshold is used to judge whether the closest old MPC/cluster can be treated as a new MPC/cluster. This threshold is mainly determined by the resolution of measurement system in the angular and delay domain, as well as the data post-processing scheme. The value of threshold is set to 0.06 by experience and is found to produce satisfying tracking results. To address the limitations of automatic algorithms in accurately capturing small scatterer clusters, we further refine the clustering results through visual inspection. This approach effectively balances accuracy and computational efficiency, and is also used in [49], [50].

Fig. 9(b) demonstrates the result of clustering and tracking based on measured data, where each cluster is distinguished by a unique color or marker. Specifically, red circles denote LOS cluster, while the remaining markers represent scatterer clusters. It can be seen that the LOS cluster is dominant and consistently present. However, limited by measurement scenario and bandwidth, although a few long-lasting and prominent clusters can be identified, the total number of distinguishable clusters is limited.

C. Time-Variant Evolution Characterization

The high mobility of high-speed trains will lead to rapid time-variant channels, which in turn leads to birth and death of clusters and rapid changes in cluster characteristics [51]. In Section II, we present a general model of non-stationarity in 5G-R channels and the birth-death process of clusters. In this subsection, we utilize cluster lifetime and a first-order four-state Markov chain to characterize birth-death process of clusters based on measured data.

1) *Number of Clusters*. The number of clusters can reflect the richness of MPCs in measurement environment [52]. We have identified a total of 20 clusters within an effective measurement period of approximately 60 seconds, including one LOS cluster and 19 NLOS clusters, as shown in Fig. 9(b). Fig. 10 illustrates the proportion of clusters observed within stationary region ΔW . It can be seen that in roughly one-third of the time, only two clusters are distinguishable, while six clusters can be identified in just 4% of the time. Additionally, five clusters are observable in about one-fifth of time, which is slightly higher than 3 and 4 clusters. This phenomenon can be attributed to two factors. First, the relatively open measurement environment means that only certain houses or buildings along the railway act as scatterers and has low scatterer density. Second, small measurement bandwidth results in low delay resolution, making it difficult to distinguish more MPCs.

2) *Lifetime of Clusters*. The lifetime of clusters is the duration between the appearance and disappearance of each cluster. Fig. 11 shows the CDFs of cluster lifetime. It is found that cluster lifetime has a Lognormal distribution, with mean value 3.74 s and standard deviation 4.57 s. It is seen that 80% of clusters have a lifetime of less than 5 seconds, indicating that most scatterers are relatively small in size. However, a few clusters exhibit longer lifetimes, ranging from 15 to 20

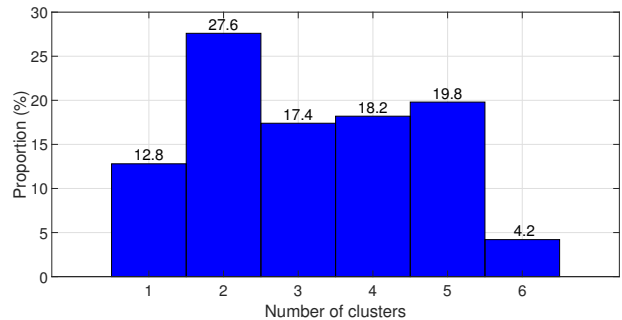


Fig. 10. The count histogram of the cluster number within stationary region ΔW .

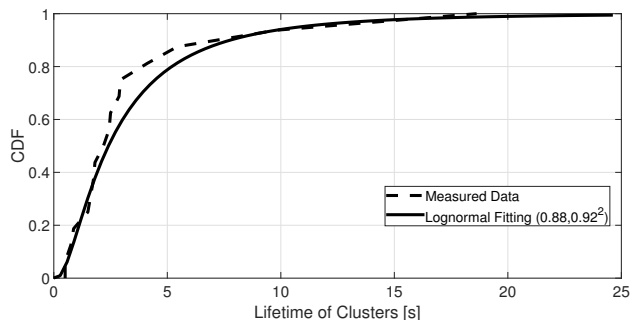


Fig. 11. The CDFs of cluster lifetime.

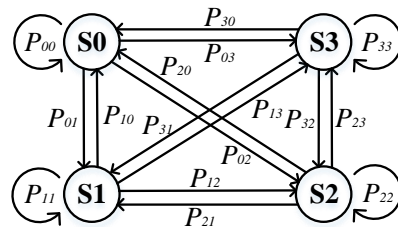


Fig. 12. First-order four-state Markov chain.

seconds. This is due to the presence of larger structures, such as control rooms and operation and maintenance facilities along the railway, which can be observed from Fig. 3.

3) *Markov chain*. Markov chains are often used to characterize the evolution of dynamic clusters [53], [54]. In order to analyze birth-death process of dynamic clusters, a first-order four-state Markov chain is considered, as shown in Fig. 12. Four typical states conform to the characteristics of 5G-R communication channel evolution. The four states are defined as S_0 (no “births” or “deaths”), S_1 (“births” only), S_2 (“deaths” only), and S_3 (both “births” and “deaths”). Based on clustering results, state transfer matrix P_T is

$$\begin{aligned}
 P_T = \{p_{ij}\} &= \begin{bmatrix} P_{00} & P_{01} & P_{02} & P_{03} \\ P_{10} & P_{11} & P_{12} & P_{13} \\ P_{20} & P_{21} & P_{22} & P_{23} \\ P_{30} & P_{31} & P_{32} & P_{33} \end{bmatrix} \\
 &= \begin{bmatrix} 0.66 & 0.16 & 0.12 & 0.06 \\ 0.28 & 0.02 & 0.53 & 0.17 \\ 0.36 & 0.47 & 0.05 & 0.12 \\ 0.16 & 0.13 & 0.19 & 0.52 \end{bmatrix} \quad (31)
 \end{aligned}$$

TABLE III
CDL MODEL PARAMETERS.

| Model | 5G-R Rural | | | | 3GPP RMa CDL-D [31] | | | |
|------------|------------|------------|-----------|-----------|---------------------|------------|-----------|-----------|
| | Delay [ns] | Power [dB] | AOA [deg] | EOA [deg] | Delay [ns] | Power [dB] | AOA [deg] | EOA [deg] |
| 1 (LOS) | 0 | -0.5 | 219.6 | 65.5 | 0 | -0.2 | -180 | 81.5 |
| 2 | 70.787 | -23.7 | 153.5 | 70.9 | 5.497 | -18.8 | 89.2 | 86.9 |
| 3 | 180.345 | -20.9 | 166.6 | 66.8 | 96.123 | -21 | 89.2 | 86.9 |
| 4 | 282.813 | -11.4 | 153.5 | 65.2 | 214.08 | -22.8 | 89.2 | 86.9 |
| 5 | 806.152 | -15.1 | 66.2 | 64.5 | 220.674 | -17.9 | 163 | 79.4 |

where i and j represent the state index, while p_{ij} is the transition probability from state S_i to state S_j . It can be observed that for initial state S_0 , its next state is most likely to remain at S_0 with a high probability, as indicated by the largest transition probability P_{00} . It implies that, in the absence of cluster birth or death, next state will most likely continue without any cluster birth or death, corresponding to the first half of Fig. 9, where only LOS cluster and a few long-lasting NLOS clusters are present. For initial states S_1 , S_2 and S_3 , there is approximately a 50% chance that they will transition sequentially to states S_2 , S_1 and S_3 respectively, which means that when cluster birth or death occurs, the subsequent state is highly likely to be the opposite state or remain unchanged. This indicates a relatively high density of clusters, with a more uniform spatial distribution, which aligns with the second half of Fig. 9, reflecting the presence of numerous and short-duration scatterers. The above phenomenon can also be clearly observed in measurement scenario as shown in Fig. 3. There are few low-rise buildings such as houses in area A, but larger railway-specific structures dominate the environment, whereas in area B, the presence of denser housing results in the frequent birth and death of clusters.

VI. MODEL IMPLEMENTATION AND VALIDATION

A. Measurement-Based CDL Channel Model

In Sections IV and V, we have obtained sufficient channel characteristics and MPC cluster characteristics. Next, we establish the CDL model of 5G-R channel according to standard procedure of 3GPP TR 38.901 [31]. Five CDL models are mentioned in [31], and the widely used CDL-D model in [45], [55] for LOS scenarios are selected as the standard. There are 13 clusters are defined in CDL-D model, but such a large number of clusters cannot be obtained based on measurements. As illustrated in Fig. 10, within stationary region, we can identify a maximum of 6 clusters with the lowest proportion. While the 2 clusters have the highest proportion, it is not sufficient for developing a generalized CDL model. Therefore, we choose the scenario with 5 clusters, which represents the second most frequent case, to construct CDL model. Following the procedure in Section II, we merge the identified clusters and calculate the delays, powers, AOAs and EOAs, in accordance with the CDL-D model. Since the 3GPP RMa scenario is similar to test environment, we herein incorporate its CDL model as a comparison. The parameters of established

CDL model and the first five clusters in CDL-D model are presented in Table III.

For comparison, we scale normalized delay in CDL-D model by applying a scaling factor for RMa scenario to obtain scaled delay, while other parameters are calculated following 3GPP. We find that the proposed 5G-R CDL model has several differences from 3GPP CDL-D model. First, from the perspective of delay, cluster delay in 5G-R model is significantly larger than 3GPP model, suggesting that the measurement scenario involves more distant scatterers. In addition to the difference in measurement scenarios, this phenomenon may also be attributed to the limited delay resolution, which is only 100 nanoseconds, making it difficult to fully distinguish LOS path and MPCs close to it. Therefore, MPCs that can be distinguished are far away from LOS path and have a substantially larger relative delay. As for power, it can be found that LOS cluster in 5G-R model has a lower power value compared to 3GPP model, indicating that more power is allocated to NLOS clusters. It can be explained in Fig. 9(b), which shows that when LOS cluster is positioned directly below BS, its energy is more dispersed, and a portion of energy is distributed to NLOS clusters. This may be the reason why the power of 4th and 5th clusters is still high even though the delay is large. AOA and EOA are highly scenario-dependent. Since both models are rural scenarios, their overall trends of angles are consistent, though there are slight variations in specific values. For example, values of EOA fluctuate between $64^\circ-71^\circ$ and $79^\circ-87^\circ$ in both models, respectively. This indicates that in rural scenario, EOA changes remain relatively stable, while AOA, in contrast, shows more significant fluctuations, even spanning up to 180° .

B. Model Validation

In this paper, three second-order statistics, i.e., RMS DS, ASA and ESA, and stationarity distance are used to validate the proposed 5G-R time-variant model. To compare with measured data, we set antenna height, positions and other general simulation parameters to be the same as in measurements. The generation of channel coefficients follows the process in Section II. Note that multiple sets of data are obtained during measurements. Part of the dataset is used for statistical analysis and modeling, while the rest is used for model validation.

The CDFs of RMS DS, AS, stationarity distance between simulated, measured and 3GPP channels are shown in Fig. 13,

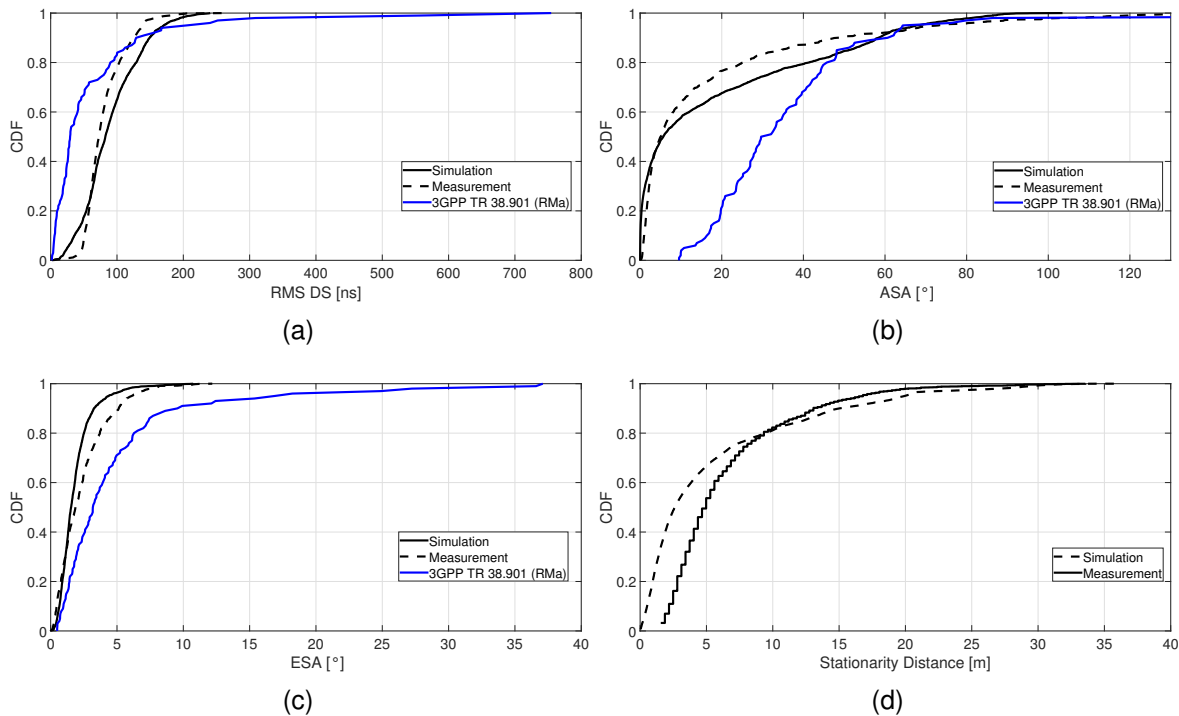


Fig. 13. Model comparisons between simulated and measured channels. (a) RMS DS. (b) ASA. (c) ESA. (d) Stationarity distance.

respectively. Note that since 3GPP lacks parameterization for describing non-stationarity, a comparison with 3GPP model in Fig. 13(d) is not possible. However, 3GPP model is included for comparison alongside simulations and measurements in the other three subfigures. Due to the positions of scatterers in simulation are randomly generated, the resulting channel parameters cannot fully align with the measurements, even though the UT parameters are configured to match the measurements as closely as possible. Nevertheless, the overall agreement is fairly good and reasonable. In contrast, the fitting results of 3GPP channel and measured channel are quite different. This clearly shows that the proposed model has improved performances than 3GPP model, making it more consistent with actual dynamic channel conditions.

VII. CONCLUSION

In this paper, we present a cluster-based time-variant channel model for 5G-R within an enhanced 3GPP framework, incorporating time evolution to capture dynamic channel characteristics. Extensive channel measurements are conducted on 5G-R private network test line of China, providing a rich measured data for analysis. We then analyze typical channel fading characteristics, such as PL, RMS DS, AOA, etc. Additionally, we extract MPCs using KPowerMeans algorithm combined with MCD-based tracking algorithm, allowing us to characterize clusters with high precision. Next, birth-death process of cluster is modeled and analyzed utilizing cluster lifetime and a first-order four-state Markov chain. Finally, we develop a generalized CDL model in accordance with 3GPP standard and validate its accuracy by comparing measurement and simulation results, and the model has been proven to

have improved performances than 3GPP. This work enhances the understanding of 5G-R channels and will significantly contribute to the design, deployment, and optimization of 5G-R networks.

REFERENCES

- [1] X. Zhang *et al.*, "Measurement-based channel characterization and modeling for 5G-Railways at 2.16 GHz," in *Proc. IEEE 16th Int. Conf. Wireless Commun. Signal Process. (WCSP)*, 2024, pp. 1–6, accepted.
- [2] R. He *et al.*, "High-speed railway communications: From GSM-R to LTE-R," *IEEE Veh. Technol. Mag.*, vol. 11, no. 3, pp. 49–58, 2016.
- [3] C. Liu *et al.*, "Reconfigurable intelligent surface assisted high-speed train communications: Coverage performance analysis and placement optimization," *IEEE Trans. Veh. Technol.*, vol. 73, no. 3, pp. 3750–3766, 2024.
- [4] B. Ai, A. F. Molisch, M. Rupp, and Z.-D. Zhong, "5G key technologies for smart railways," *Proc. IEEE*, vol. 108, no. 6, pp. 856–893, 2020.
- [5] R. He *et al.*, "5G for railways: Next generation railway dedicated communications," *IEEE Commun. Mag.*, vol. 60, no. 12, pp. 130–136, 2022.
- [6] R. He and B. Ai, *Wireless Channel Measurement and Modeling in Mobile Communication Scenario: Theory and Application*. CRC Press, 2024.
- [7] R. He *et al.*, "Radio communication scenarios in 5G-railways," *China Commun.*, vol. 20, no. 9, pp. 235–246, 2023.
- [8] 5GRail, "European union horizon 2020 research and innovation programme," 2020. [Online]. Available: <https://5grail.eu/>
- [9] H. Feng, S. Li, X. Ma, and M. Xu, "Development of 5G-R system in chinese railway," in *Proc. IEEE 6th Adv. Inf. Technol., Electron. Autom. Control Conf. (IAEAC)*, 2022, pp. 950–954.
- [10] R. Chen, W.-X. Long, G. Mao, and C. Li, "Development trends of mobile communication systems for railways," *IEEE Commun. Surveys Tuts.*, vol. 20, no. 4, pp. 3131–3141, 2018.
- [11] Y. Liang, H. Li, Y. Li, and A. Li, "Mainline railway modeled with 2100 MHz 5G-R channel based on measured data of test line of loop railway," *Symmetry*, vol. 16, no. 4, p. 431, 2024.
- [12] X. Zhang, R. He, M. Yang, Z. Qi, Z. Zhang, B. Ai, and R. Chen, "Narrowband channel measurements and statistical characterization in subway tunnels at 1.8 and 5.8 GHz," *IEEE Trans. Veh. Technol.*, vol. 73, no. 7, pp. 10 228–10 240, 2024.

- [13] Z. Zhang *et al.*, "A cluster-based statistical channel model for integrated sensing and communication channels," *IEEE Trans. Wireless Commun.*, vol. 23, no. 9, pp. 11597–11611, 2024.
- [14] T. Zhou, H. Zhang, B. Ai, C. Xue, and L. Liu, "Deep-learning-based spatial-temporal channel prediction for smart high-speed railway communication networks," *IEEE Trans. Wireless Commun.*, vol. 21, no. 7, pp. 5333–5345, 2022.
- [15] F. Hu, Z. Ling, T. Liu, H. Li, and B. Ai, "Wireless perception of high-speed railway communication: Challenges, framework, and future directions," *IEEE Wireless Commun.*, vol. 31, no. 4, pp. 284–292, 2024.
- [16] R. He, Z. Zhong, B. Ai, G. Wang, J. Ding, and A. F. Molisch, "Measurements and analysis of propagation channels in high-speed railway viaducts," *IEEE Trans. Wireless Commun.*, vol. 12, no. 2, pp. 794–805, 2013.
- [17] R. He, Z. Zhong, B. Ai, J. Ding, Y. Yang, and A. F. Molisch, "Short-term fading behavior in high-speed railway cutting scenario: Measurements, analysis, and statistical models," *IEEE Trans. Antennas Propag.*, vol. 61, no. 4, pp. 2209–2222, 2013.
- [18] T. Zhou, C. Tao, S. Salous, and L. Liu, "Measurements and analysis of short-term fading behavior in high-speed railway communication networks," *IEEE Trans. Veh. Technol.*, vol. 68, no. 1, pp. 101–112, 2019.
- [19] T. Zhou, H. Li, Y. Wang, L. Liu, and C. Tao, "Channel modeling for future high-speed railway communication systems: A survey," *IEEE Access*, vol. 7, pp. 52818–52826, 2019.
- [20] B. Zhang *et al.*, "Measurement-based markov modeling for multi-link channels in railway communication systems," *IEEE Trans. Intell. Transp. Syst.*, vol. 20, no. 3, pp. 985–999, 2019.
- [21] L. Liu, C. Tao, R. Sun, H. Chen, and Z. Lin, "Markov chain based channel characterization for high speed railway in viaduct scenarios," in *Proc. IEEE Int. Conf. Commun. (ICC)*, 2014, pp. 5896–5901.
- [22] L. Liu *et al.*, "Non-stationary channel characterization for high-speed railway under viaduct scenarios," *Chin. Sci. Bull.*, vol. 59, pp. 4988–4998, 2014.
- [23] J. Qiu, C. Tao, L. Liu, Z. Lin, and Z. Tan, "A novel hybrid CDL-based multipath propagation model for the high-speed railway at 2.35 GHz," *Chin. Sci. Bull.*, vol. 59, pp. 4976–4987, 2014.
- [24] J. DING, Y. LIU, H. LIAO, B. SUN, and W. WANG, "Statistical model of path loss for railway 5G marshalling yard scenario," *ZTE Commun.*, vol. 21, no. 3, p. 117, 2023.
- [25] D. He *et al.*, "Ray-tracing simulation and analysis of propagation for 3GPP high speed scenarios," in *Proc. 11th Eur. Conf. Antennas Propag. (EuCAP)*, 2017, pp. 2890–2894.
- [26] T. Liu, D. He, K. Guan, D. Liu, and F. Zhu, "Channel characterization for 5G-R indoor communication at 2.1 GHz," in *Proc. 16th Eur. Conf. Antennas Propag. (EuCAP)*, 2022, pp. 01–05.
- [27] X. Cheng, Z. Huang, and L. Bai, "Channel nonstationarity and consistency for beyond 5G and 6G: A survey," *IEEE Commun. Surveys Tuts.*, vol. 24, no. 3, pp. 1634–1669, 2022.
- [28] Y. Liu, L. Feng, J. Sun, W. Zhang, C.-X. Wang, and P. Fan, "3D non-stationary GBMS for high-speed train tunnel channels," in *Proc. IEEE 87th Veh. Technol. Conf. (VTC Spring)*, Porto, Portugal, Jun. 2018, pp. 1–5.
- [29] Y. Feng, R. Wang, G. Zheng, A. Saleem, and W. Xiang, "A 3D non-stationary small-scale fading model for 5G high-speed train massive MIMO channels," *IEEE Trans. Intell. Transp. Syst.*, pp. 1–16, 2024.
- [30] I. Winner, "WINNER II channel models," *IST-4-027756*, 2007.
- [31] 3GPP, "Study on channel model for frequencies from 0.5 to 100 GHz (release 18)," *Tech. Rep. 38.901, V18.0.0*, Mar. 2024.
- [32] L. Liu *et al.*, "The COST 2100 MIMO channel model," *IEEE Wireless Commun.*, vol. 19, no. 6, pp. 92–99, 2012.
- [33] S. Jaeckel, L. Raschkowski, K. Börner, and L. Thiele, "QuadRiGa: A 3-D multi-cell channel model with time evolution for enabling virtual field trials," *IEEE Trans. Antennas Propag.*, vol. 62, no. 6, pp. 3242–3256, 2014.
- [34] M. Series, "Guidelines for evaluation of radio interface technologies for imt-2020," *Report ITU*, vol. 2512, no. 0, 2017.
- [35] C. Wang, J. Zhang, and G. Yu, "Cluster analysis of pedestrian mobile channels in measurements and simulations," *Appl. Sci.*, vol. 9, no. 5, 2019.
- [36] J. Bian, J. Sun, C.-X. Wang, R. Feng, J. Huang, Y. Yang, and M. Zhang, "A WINNER+ based 3-D non-stationary wideband MIMO channel model," *IEEE Trans. Wireless Commun.*, vol. 17, no. 3, pp. 1755–1767, 2018.
- [37] Y. Jin and D. Wang, "Study on static deflection model of MEMS capacitive microwave power sensors," *Chinese J Electron*, vol. 33, no. 5, pp. 1188–1195, 2024.
- [38] H. Chang, C.-X. Wang, Y. Liu, J. Huang, J. Sun, W. Zhang, Z. Bai, K. An, Z. Li, and E.-H. M. Aggoune, "A general 3-D nonstationary GBMS for underground vehicular channels," *IEEE Trans. Antennas Propag.*, vol. 71, no. 2, pp. 1804–1819, 2023.
- [39] S. Wu, C.-X. Wang, e.-H. M. Aggoune, M. M. Alwakeel, and X. You, "A general 3-D non-stationary 5G wireless channel model," *IEEE Trans. Commun.*, vol. 66, no. 7, pp. 3065–3078, 2018.
- [40] R. He, B. Ai, G. Wang, M. Yang, C. Huang, and Z. Zhong, "Wireless channel sparsity: Measurement, analysis, and exploitation in estimation," *IEEE Wireless Commun.*, vol. 28, no. 4, pp. 113–119, 2021.
- [41] M. Yang *et al.*, "V2V channel characterization and modeling for underground parking garages," *China Commun.*, vol. 16, no. 9, pp. 93–105, 2019.
- [42] X. Zhang *et al.*, "Measurements and modeling of large-scale channel characteristics in subway tunnels at 1.8 and 5.8 GHz," *IEEE Antennas Wireless Propag. Lett.*, vol. 22, no. 3, pp. 561–565, 2023.
- [43] M. Yang *et al.*, "Dynamic V2V channel measurement and modeling at street intersection scenarios," *IEEE Trans. Antennas Propag.*, vol. 71, no. 5, pp. 4417–4432, May 2023.
- [44] Y. Fan *et al.*, "Measurements and characterization for the vehicle-to-infrastructure channel in urban and highway scenarios at 5.92 GHz," *China Commun.*, vol. 19, no. 4, pp. 28–43, 2022.
- [45] Z. Cui, K. Guan, C. Oestges, C. Briso-Rodríguez, B. Ai, and Z. Zhong, "Cluster-based characterization and modeling for UAV air-to-ground time-varying channels," *IEEE Trans. Veh. Technol.*, vol. 71, no. 7, pp. 6872–6883, 2022.
- [46] N. Czink, P. Cera, J. Salo, E. Bonek, J.-p. Nuutinen, and J. Ylitalo, "A framework for automatic clustering of parametric MIMO channel data including path powers," in *Proc. IEEE Veh. Technol. Conf.*, 2006, pp. 1–5.
- [47] R. He, O. Renaudin, V.-M. Kolmonen, K. Haneda, Z. Zhong, B. Ai, and C. Oestges, "A dynamic wideband directional channel model for vehicle-to-vehicle communications," *IEEE Trans. Ind. Electron.*, vol. 62, no. 12, pp. 7870–7882, 2015.
- [48] J. Li, B. Ai, R. He, M. Yang, Z. Zhong, and Y. Hao, "A cluster-based channel model for massive MIMO communications in indoor hotspot scenarios," *IEEE Trans. Wireless Commun.*, vol. 18, no. 8, pp. 3856–3870, 2019.
- [49] J. Li *et al.*, "Cluster-based 3-D channel modeling for massive mimo in subway station environment," *IEEE Access*, vol. 6, pp. 6257–6272, 2018.
- [50] M. Yang *et al.*, "Measurements and cluster-based modeling of vehicle-to-vehicle channels with large vehicle obstructions," *IEEE Trans. Wireless Commun.*, vol. 19, no. 9, pp. 5860–5874, 2020.
- [51] X. Zhao *et al.*, "Semi-deterministic dynamic millimeter-wave channel modeling based on an optimal neural network approach," *IEEE Trans. Antennas Propag.*, vol. 70, no. 6, pp. 4082–4095, 2022.
- [52] M. Yang *et al.*, "A cluster-based three-dimensional channel model for vehicle-to-vehicle communications," *IEEE Trans. Veh. Technol.*, vol. 68, no. 6, pp. 5208–5220, 2019.
- [53] Z. Zhang, Y. Liu, C.-X. Wang, H. Chang, J. Bian, and J. Zhang, "Machine learning based clustering and modeling for 6G UAV-to-ground communication channels," *IEEE Trans. Veh. Technol.*, pp. 1–14, 2024.
- [54] T. Zhou, Y. Qiao, S. Salous, L. Liu, and C. Tao, "Machine learning-based multipath components clustering and cluster characteristics analysis in high-speed railway scenarios," *IEEE Trans. Antennas Propag.*, vol. 70, no. 6, pp. 4027–4039, 2022.
- [55] A. M. Pessoa, B. Sokal, C. F. M. E. Silva, T. F. Maciel, A. L. F. De Almeida, and F. R. P. Cavalcanti, "A CDL-based channel model with dual-polarized antennas for 5G MIMO systems in rural remote areas," *IEEE Access*, vol. 8, pp. 163366–163379, 2020.
- [56] Z. Zhang *et al.*, "A cluster-based statistical channel model for integrated sensing and communication channels," *IEEE Trans. Wireless Commun.*, pp. 1–1, 2024.
- [57] C. Luo, A. Tang, F. Gao, J. Liu, and X. Wang, "Channel modeling framework for both communications and bistatic sensing under 3GPP standard," *IEEE J. Sel. Areas Sensors*, pp. 1–11, 2024.
- [58] Z. Fu, H. Cui, X. Zhao, Y. Wang, Z. Wang, L. Qiu, and Y. Wang, "An improved CDL model for 5G millimeter wave communication in a substation scenario," in *Proc. IEEE/CIC Int. Conf. Commun. China (ICCC Workshops)*, 2020, pp. 18–22.
- [59] D. G. Riviello, F. Di Stasio, and R. Tuninato, "Performance analysis of multi-user MIMO schemes under realistic 3GPP 3-D channel model for 5G mmwave cellular networks," *Electronics*, vol. 11, no. 3, pp. 1–28, 2022.